Wear 376-377 (2017) 738–746

Contents lists available at ScienceDirect

Wear

journal homepage: www.elsevier.com/locate/wear

An energy approach for impact wear in water environment

Thibaut Souilliart [a,b,*], Emmanuel Rigaud [a], Alain Le Bot [a], Christian Phalippou [b]

[a] Laboratoire de Tribologie et Dynamique des Systèmes, UMR CNRS 5513, Ecole Centrale de Lyon, Université de Lyon, 36 avenue Guy de Collongue, 69134 Ecully, France

[b] Commissariat à l'Energie Atomique et aux Energies Alternatives CEA-Saclay, DEN, DANS, DM2S, SEMT, DYN, F-91191 Gif-sur-Yvette, France

ARTICLE INFO

Article history:
Received 2 September 2016
Received in revised form
25 November 2016
Accepted 1 December 2016

Keywords:
Impact wear
Sliding distance
Friction coefficient
Energy of impact
Inconel 690 wear
Lubricated friction

ABSTRACT

Wear induced by repetitive impacts between steam generator tubes and anti-vibration bars in pressurized water reactors is studied with an analytical impact wear apparatus. Repetitive impacts between an Inconel tube sample and a stainless steel flat bar target are performed in water environment at ambient temperature. Incident energy and angle of impacts are controlled, normal and tangential loads during impact are measured as well as rebound energy and angle of impacts. Impacts characteristics are deeply analyzed and interdependences are highlighted. In particular, the evolution of restitution coefficient, ratio between tangential and normal impulses during impacts, energy loss and sliding distance during impacts versus incidence angle are identified. Impact wear is found to be strongly dependent to impact dynamics, in particular it is observed to be proportional to energy loss during impacts and dependent to incidence angle with a maximum near 20° to the tangential axis. Microscope observation of the wear scars shows the existence of numerous abrasive scratches whose length corresponds to the sliding distance during impact. An impact model is introduced to express energy loss and sliding distance as functions of incidence angle, incident energy, restitution coefficient and impulse ratio. Experimental wear is observed to be dependent on both incidence angle and energy loss.

1. Introduction

In Pressurized Water Reactors (PWR), Steam Generator (SG) tubes are subjected to repetitive impacts against Anti-Vibration Bars (AVB) which sometimes induce significant wear. When becoming too large, wear can lead to plug the SG tube. Therefore, the understanding of the wear formation processes and the analysis of the relationship between impacts characteristics and SG tube wear is a major concern for the safety of PWR.

Several types of impact wear exist according to the motions and the involved bodies [1]. Whether impacts involve substantial incident mass and low velocity (percussive impacts) or low mass and large velocity (particle erosion), two categories of wear models are proposed. Concerning percussive impact wear, Engel [2–4] proposes a model taking account of the surfaces conformance during wear formation and based on a strong dependence on the shear stress. Levy [5], Connors [6], Frick [7] and Hoffman [8] propose wear models based on a proportionality with load and sliding distance derived from Archard's equation. Lewis [9] takes over the Engel model by adding a new dependency with sliding distance. Gessesse [10] and Attia [11] extend the delamination theory of sliding wear from Suh to percussive impact wear, with a specific interest to the contact geometry at the asperity scale. Concerning erosion wear, three types of models can be distinguished [12]. Finnie [13,14] and Bitter [15] propose models for a rigid grain cutting into a ductile metal. Hutchings [16], Follansbee [17], Ratner [18] and Sundararajan [19] develop fatigue models which involve a critical accumulated strain required to generate wear. Jahanmir extends the delamination theory of sliding wear from Suh [20] to erosion wear.

Impact characteristics are deeply studied by Stronge [21]. The analysis of velocities, kinetic energy, forces, friction, stick and slip regions of the contact during impact results in a rich but complex formulation of impact characteristics. Brach [22,23] uses a classical impulse and momentum theory to express these characteristics, especially the energy loss during an impact. It leads to simpler and more intelligible formulations with a high degree of physical meaning. Brach observes a good correlation between the energy loss during an impact and erosive wear results from literature. No comparison is carried out between this model and percussive impact wear observations.

A lot of experimental studies have been carried out in the last decades about impact wear in nuclear field. Guinot [24] and Zaghdoudi [25] have listed many impact test machines and gather them into two categories whether or not priority is given to reproducing real PWR environment. Ko [26] , Cha [27] and Blevins [28] among others studied impacts and wear with real environment test machines. Sorokin [29], Rice [30] and Pick [31] developed analytical test

* Corresponding author at: Laboratoire de Tribologie et Dynamique des Systèmes, UMR CNRS 5513, Ecole Centrale de Lyon, Université de Lyon, 36 avenue Guy de Collongue, 69134 Ecully, France.

http://dx.doi.org/10.1016/j.wear.2016.12.059
0043-1648/

Nomenclature

d_n	normal contact duration: $d_n=t_{rn}-t_{in}$
d_t	tangential contact duration: $d_t=t_{rt}-t_{it}$
e	restitution coefficient of impact
f	excitation frequency
f_{Engel}	slip factor
l_s	sliding distance during impact
m	projectile mass
m_a	apparent mass seen by one contact asperity: $m_a=m/N_a$
t	time
$t_{in}; t_{it}$	time location of normal/tangential load beginning during impact
$t_{rn}; t_{rt}$	time location of normal/tangential load end during impact
$v_r; v_{rn}; v_{rt}$	rebound velocity; normal/tangential component of rebound velocity
$v_i; v_{in}; v_{it}$	incident velocity; normal/tangential component of incident velocity
D_t	tangential position of the projectile
E^*	equivalent Young modulus in Hertz theory
$F_n; F_t$	normal/tangential component of load
$F_{nm}; F_{tm}$	maximum value of normal/tangential contact load during impact
K	impact wear energy coefficient
N_a	number of contact asperities
$P_n; P_t$	normal/tangential impulse during impact
R_q	roughness parameter
T_i	incident kinetic energy of the projectile
$T_L; T_{Ln}; T_{Lt}$	energy loss; normal/tangential component of energy loss
T_L^*	normalized energy loss
$V^-; V^+$	negative/positive wear volume
V_{imp}^-	wear volume per impact
α_i	incidence angle of the projectile
α_r	rebound angle of the projectile
β	asperity radius of curvature
μ	impulse ratio
μ_c	critical impulse ratio
μ_{end}	impulse ratio at the end of wear test
μ_k	kinetic friction coefficient

machines to study normal impact only. These test machines are expected to have better characteristics than the ones which reproduce real environment but the precision of the dynamics control is very different from one apparatus to another. A lack of analytical experimental apparatus with a large range of possible incidence angles is to be noted.

In the present work, wear of a SG tube sample subjected to repetitive impacts against an AVB sample is studied in water environment. Section 2 presents the experimental apparatus that has been designed and used. Section 3 presents a detailed statistical analysis of the impacts and their characteristics. Section 4 presents an analysis of the wear scars and volumes based on topographic measurements and energy considerations.

2. Experimental details

2.1. Impact wear apparatus

The experimental apparatus has been designed to study impact wear between a SG tube sample and an AVB sample in water. A schematic representation of the test machine is presented in Fig. 1 and a picture in Fig. 2. The stationary sample (AVB bar) is mounted inside a water container (volume capacity of 20 mL) on a very stiff support. The mobile sample (SG tube) is inside a tube holder supported by two springs (stiffness k = 590 N/m) in the YZ-plane. Due to experimental choices, the tube holder restricts the ovalization of the SG tube sample. Two shakers control the motion of the mobile sample. The geometry of the contact is cylinder-plane (line contact).

A 3-axis piezoelectric sensor is placed about 40 mm under the contact region and is used to measure the normal and the tangential loads during impacts. Two laser displacement sensors centered on the center of the tube sample are used to measure the incidence and rebound parameters of each impact. The shakers excitation and the dynamic data acquisition are controlled by computer. Signals are recorded with a high sampling rate (50 kHz) to obtain high quality measurements of the contact load time evolution during impacts. An extensive study of the test apparatus stiffnesses and the corresponding eigenmodes as well as their effect on the measurement signals has been carried out in reference

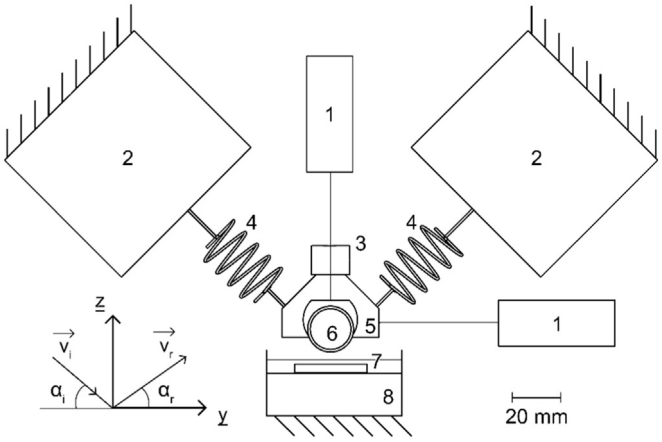

Fig. 1. Diagram of the impact wear test machine (1: Displacement sensors, 2: Shakers, 3: Loading mass, 4: Springs, 5: Tube holder, 6: SG Tube, 7: AVB holder with water container and AVB sample, 8: Force transducer).

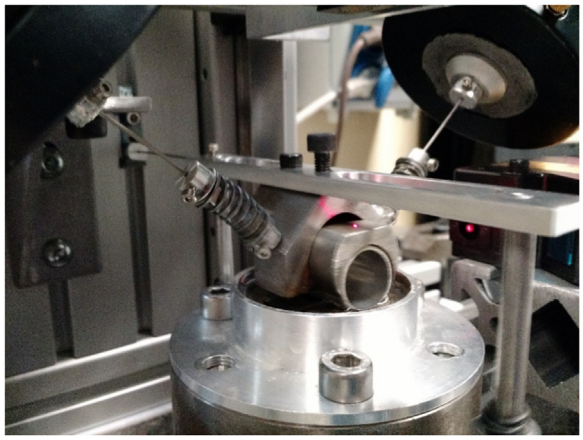

Fig. 2. Picture of the impact wear test machine.

[32]. A two-degrees-of-freedom dynamic model of the test apparatus is proposed and leads to conclude that the interface is governed by the contact asperities and the free vibration of the force

transducer has a slight influence on the force signal.

A complete time acquisition of contact loads and displacements during the full length of the test is impossible due to storage space limitation. Therefore, signals are acquired during 2000 evenly distributed acquisition time windows of 1 second.

At the end of a wear test, the worn SG tube sample is analyzed with a microscope and an optical interferometer and wear volumes are measured.

2.2. Wear specimens

The stationary sample is a AISI 410s steel flat anti vibration bar sample (13 wt% Cr, 1 wt% Si, 1 wt% Mn and 85 wt% Fe) of 12 mm width. The mobile sample is an Inconel 690 SG tube sample (31 wt% Cr, 10 wt% Fe and 59 wt% Fe) of 19.05 mm external diameter, 1.09 mm thickness and 35 mm long. The samples used in this study are extracted from real components in order to obtain a good representativeness of the wear tests.

2.3. Experimental conditions

The influence of the impact dynamics is studied by varying the incidence angle α_i and the incidence energy T_i of the impacts from a wear test to another. During each test, the incidence angle and the incidence kinetic energy are controlled to be constant. The standard test duration is 20 h and the excitation frequency f is 20 Hz so that the total number of impacts is about 1.4 million. The tests are carried out at ambient temperature and in distilled water. The water environment has been chosen to obtain a better representativeness of the wear tests to the PWR context of this study. The first tests campaign aims at studying the influence of the incidence angle on wear in the range 5°–85°. During these tests, the incidence kinetic energy is controlled to be equal to 0.35 mJ, corresponding to an incident velocity of 70 mm/s. The second tests campaign aims at studying the influence of the incidence energy on wear in the range 0.05–1 mJ. During these tests, the incidence angle is controlled to be equal to 30° from the horizontal.

Sweep tests have also been carried out in order to analyze more precisely the interdependence between impacts characteristics. During these tests, an incidence angle sweep is carried with a constant incident energy of 0.35 mJ, an excitation frequency of 20 Hz and a test duration of 1600 s. The incidence angle varies from 85° at t=0 s to 5° at t=1600 s (the results are repeatable if done in reverse order). The short duration of these tests allows to avoid the potential scattering of the measurements linked to the contact geometry modification as wear is generated during long tests. Similar sweep tests are carried with a varying incident energy from 0.05 mJ to 1 mJ and a constant incidence angle equal to 30°. The experimental results from the sweep tests are used to present the analysis of the impacts of Section 3.

3. Statistical analysis of the impacts

Impact wear is associated with dissipation. Several mechanical parameters are commonly used in the literature [1] to describe this dissipation. Among them one finds the restitution coefficient, impulse ratio, sliding distance, energy loss and in particular the tangential component of energy loss. Each of these parameters are deeply analyzed in the following in order to be correlated with wear in the next section.

3.1. Impact characteristics

Measured loads and displacements are processed to calculate the relevant parameters of impacts. The normal and tangential velocities before the impact v_{in} and v_{it} and after the impact $v_{rn}$and v_{rt} are deduced from displacements. The incidence angle α_i and the rebound angle α_r of the mobile sample are calculated as follows:

$$\alpha_i=\tan^{-1}\left|\frac{v_{in}}{v_{it}}\right| \tag{1}$$

$$\alpha_r=\tan^{-1}\left|\frac{v_{rn}}{v_{rt}}\right| \tag{2}$$

The convention adopted in this study defines that the incidence angle is 0° for pure horizontal incidence and 90° for normal impacts. The tangential and the normal components of the energy loss T_L during an impact are also calculated from the measured velocities:

$$T_{Lt}=\frac{1}{2}m\left(v_{it}^2-v_{rt}^2\right) \tag{3}$$

$$T_{Ln}=\frac{1}{2}m\left(v_{in}^2-v_{rn}^2\right) \tag{4}$$

and the total loss is $T_L=T_{Lt}+T_{Ln}$. The dimensionless energy loss T_L^* is defined by $T_L^*=T_L/T_i$ where T_i is the incident kinetic energy of the projectile.

The restitution coefficient e is identified from normal velocities:

$$e=-\frac{v_{rn}}{v_{in}} \tag{5}$$

The normal and tangential impulses are calculated by integrating the measured loads over the contact duration,

$$P_t=\int_{t_{it}}^{t_{rt}}F_t(t)dt=m(v_{rt}-v_{it}) \tag{6}$$

$$P_n=\int_{t_{in}}^{t_{rn}}F_n(t)dt=m(v_{rt}-v_{it}) \tag{7}$$

and an impulse ratio μ is introduced:

$$\mu=\frac{P_t}{P_n} \tag{8}$$

The sliding distance l_s during an impact is calculated from the measurement of the tangential displacement between the beginning and the end of the impact:

$$l_s=\left|D_t(t_{rt})-D_t(t_{it})\right| \tag{9}$$

3.2. Restitution during impacts

Fig. 3 displays restitution coefficient e versus incidence angle α_i for data measured during a sweep test. Each point of the cloud corresponds to a single impact. 32,000 impacts are performed during a sweep test. The range of abscissa values is divided in ten equal parts. Error bars are estimated for each part and correspond to standard deviations of abscissa values for horizontal bars and ordinate values for vertical bars. It can be observed that the restitution coefficient slightly increases from 0.85 to 0.95 when incidence angle increases from 5° to 85°. The more grazing the incidence angle is, the more scattered the experimental values of restitution coefficient are. This can be explained as small incidence angles lead to lower normal velocities and larger measurement errors. It can also be due to a more significant influence of the

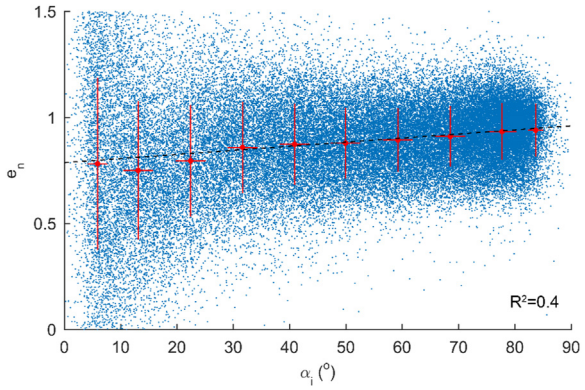

Fig. 3. Restitution coefficient vs incidence angle during impacts in water environment. Cloud: experimental data; broken black curve: linear fit.

surface topography on the rebound characteristics at small angles. The dashed black line corresponds to a linear fit defined by:

$$e(\alpha_i)=1.3\quad 10^{-3}\alpha_i+0.83 \tag{10}$$

where α_i is in degrees. The observed values of restitution coefficient are in the same order of magnitude of previous observations carried in the same incidence velocity range [33]. A study performed with the same impact test machine in dry environment shows that the restitution coefficient has slightly lower values in air than in water and ranges from 0.6 to 0.9 depending on the incidence angle [32].

Experimental results from energy sweep tests show that the restitution coefficient is constant with the incident energy in the range 0.05–1 mJ.

3.3. Friction during impacts

Fig. 4 displays the experimental impulse ratio μ defined in Eq. (8) versus incidence angle α_i for data measured during a sweep test. The dots color from blue to yellow corresponds to the rebound angle for small rebound angles (blue) to normal rebound (yellow). The impulse ratio decreases from 0.4 to 0.1 and the rebound angle increases from 0° to 90° when the incidence angle increases from 0° to 85°. The impulse ratio follows a piecewise linear decrease with a slope depending on the incidence angle range:

$$\mu=-2.1\quad 10^{-3}\alpha+0.41,\quad 0<\alpha<65° \tag{11}$$

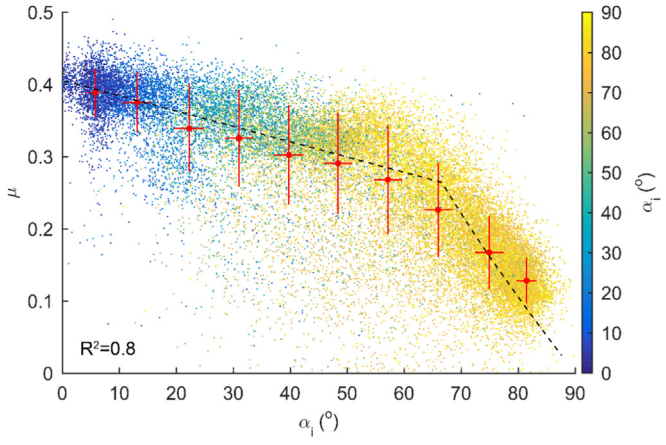

Fig. 4. Impulse ratio vs incidence angle during impacts in water environment. Cloud: experimental data; dotted curve computed from Eq. (16).

$$\mu=-6.8\quad 10^{-3}\alpha+0.71,\quad 65<\alpha<85° \tag{12}$$

In the range of incidence angle 0°–65°, the rebound angle increases from 0° to 65°. In the range 65°–85°, the rebound angle is constant and equal to 90°.

The critical impulse ratio μ_c defined by Brach [22] is introduced. In our case it is given by:

$$\mu_c=\frac{1}{1+e}\frac{1}{\tan\ \alpha_i} \tag{13}$$

This critical impulse ratio corresponds to the upper bound of an impact impulse ratio. It is interesting to note that this ratio corresponds to the slip factor f_{Engel} introduced by Engel [2] in a different way but with the same meaning:

$$f_{Engel}<2 \Leftrightarrow \mu>\mu_c \tag{14}$$

If $\mu<\mu_c$, there is sliding during all the impact and therefore μ is equal to the usual kinetic friction coefficient μ_k. The case $\mu=\mu_c$ corresponds to impacts for which the tangential velocity v_{rt} falls to zero in the contact phase. Following Eq. (2), this case induces normal rebound angles.

A critical incidence angle α_c is introduced and corresponds to the threshold between the two friction regimes described previously:

$$\alpha_c=\tan^{-1}\left(\frac{1}{\mu_k}\frac{1}{1+e}\right) \tag{15}$$

The dotted black curve in Fig. 4 corresponds to the following model:

$$\mu(\alpha_i)=\begin{cases}\mu_k(\alpha_i),\ 0°\le\alpha_i\le\alpha_c\\ \mu_c(\alpha_i),\ \alpha_i\ge\alpha_c\end{cases} \tag{16}$$

where μ_c is calculated from Eq. (13) with the value of restitution coefficient from Eq. (10), the critical incidence angle α_c is calculated from Eq. (15) and equals α_c=65°, and μ_k corresponds to the linear fit of the experimental values of Eq. (11).

A good correlation is observed between the experimental results and the model. In particular, the critical incidence angle α_c is well predicted and the evolution of the impulse ratio in the case $\alpha_i\ge\alpha_c$ is consistent with the critical impulse ratio defined by Brach [22] and Engel [2] as well as their description of the rebound behavior in this range: normal rebound angles are observed in the case $\mu=\mu_c$.

Experimental results from energy sweep tests show that the impulse ratio is constant with the incident energy in the range 0.05–1 mJ.

3.4. Energy loss during impacts

Fig. 5 shows total dimensionless energy loss T_L^* and tangential energy loss T_{Lt}^* during impacts in water environment versus incidence angle α_i. These energy losses are calculated for each impact from the measurements of incidence and rebound velocities using Eqs. (3) and (4). The mean values of the total dimensionless energy loss T_L^* increase from 0 to 0.5 when incidence angle increases from 0° to 37°. A maximum of total energy loss is observed at the incidence angle of 37°. The total energy loss decreases in the range of incidence angle 37°–80° to reach 0.2 at 80°. A similar evolution is observed for the tangential component of the energy loss T_{Lt}^* versus incidence angle: the experimental values increase from 0 to 0.43 in the range 0°–37° and decrease from 0.43 to 0 in the range 37°–90°.

Using Eqs. (1–7), the dimensionless energy loss during impacts T_L^* and its tangential component T_{Lt}^* can be expressed as a function of incidence angle α_i, and the common coefficients: restitution coefficient e and impulse ratio μ [22]. This formulation allows to

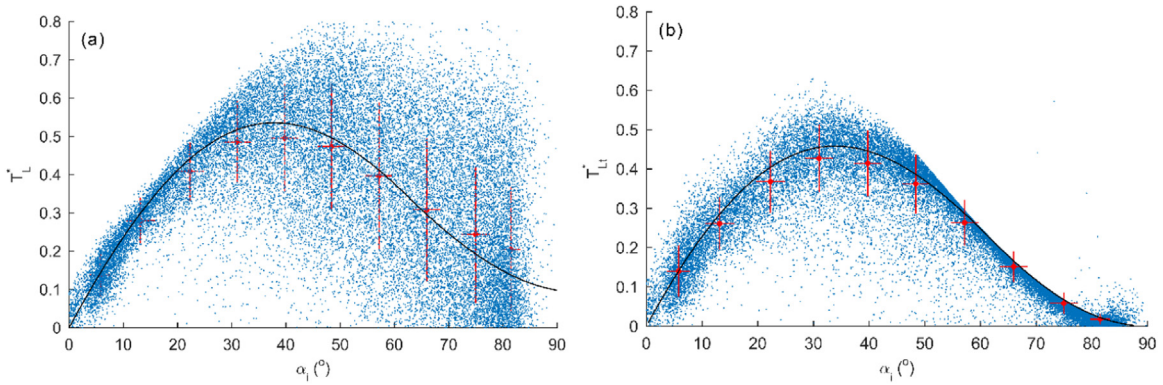

Fig. 5. (a) Total dimensionless energy loss T_L^* versus incidence angle α_i during impacts in water environment. (b) Tangential dimensionless energy loss T_{Lt}^* versus incidence angle α_i during impacts in water environment. Cloud: experimental data; solid black line respectively computed from Eqs. (17) and (18).

eliminate rebound characteristics of impacts which are unknowns:

$$T_L^*(\alpha_i, e, \mu)=(T_{Lt}+T_{Ln})/T_i=\sin^2\alpha_i(1+e)\left[1-e+\frac{2\mu}{\tan\alpha_i}-\mu^2(1+e)\right] \quad (17)$$

$$T_{Lt}^*(\alpha_i, e, \mu)=T_{Lt}/T_i=\sin^2\alpha_i(1+e)\left[\frac{2\mu}{\tan\alpha_i}-\mu^2(1+e)\right] \quad (18)$$

The solid black curves in Fig. 5 are calculated from Eqs. (17) and (18) in which the values of restitution coefficient e and impulse ratio μ are calculated with respectively Eqs. (10) and (16). A good correlation is observed between the mean values of the experimental results and the formulation of the energy losses defined by Eqs. (17) and (18). These results extend the validity of the formulation originally proposed for single erosive particle by Brach [22,23] to the case of percussive multi-asperities contacts. Nevertheless, the total experimental energy loss is much scattered in the range 37°–80° which is related to the scattering of the normal energy loss. This scattering may be related to a more significant influence of the asperity-asperity contact characteristics in this range of incident angles.

3.5. Sliding distance during impacts

The sliding distance l_s during impacts is estimated by Eq. (9). Fig. 6 displays experimental sliding distance versus incidence angle during a sweep test in water environment. The sliding distance decreases from 25 μm to 2 μm when the incidence angle increases from 0° to 85° in a quasi linear evolution. The dotted line corresponds to a linear fit of the experimental values. Fig. 7 displays sliding distance during impacts versus incident energy for several wear tests carried at incident energies ranging from 0.1 mJ to 1.2 mJ and at a constant incidence angle equal to 30°. The experimental sliding distance increases from 0 to 27 μm as the incident energy increases from 0 to 1.1 mJ.

In numerous impact wear studies, the sliding distance during the impacts is considered as a parameter with a significant influence on wear [7,9,34–36]. But in most cases, the sliding distance during impacts is neither measured nor predicted but is assumed to be proportional to the impact duration. The sliding distance during impacts and the impact duration are two unknowns and not input parameters in an impact problem. A model of the sliding distance during impact l_s defined in Eq. (9) is proposed in order to express it as a function of incident impact characteristics only, material properties and the usual coefficients: restitution coefficient e and impulse ratio

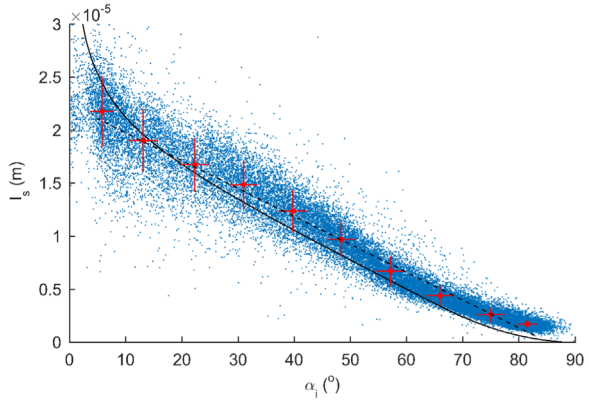

Fig. 6. Sliding distance versus incidence angle α_i during impacts in water environment. Cloud: experimental data; solid line computed from Eq. (26); dotted line: linear fit of the experimental values.

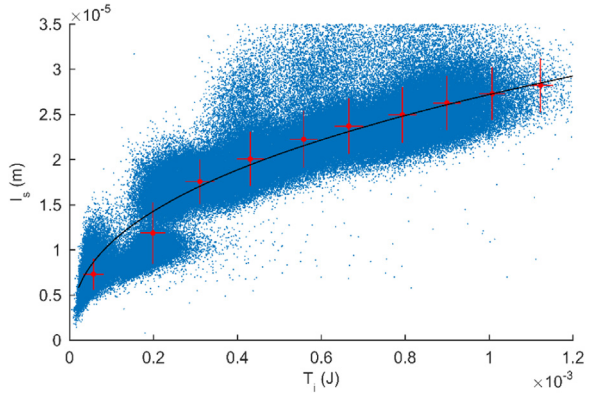

Fig. 7. Sliding distance versus incidence energy T_i during impacts in water environment at constant incidence angle equal to 30°. Cloud: experimental data; solid black line computed from Eq. (26).

μ. The following assumptions are adopted:

1) The sliding velocity varies linearly during the impact.
2) There is no stick period during the contact.
3) The normal and tangential contact loads are approximated by a sinusoidal evolution:

$$F_t=F_{tm}\sin\left(\frac{\pi}{d_t}t\right) \quad (19)$$

$$F_n=F_{nm}\sin\left(\frac{\pi}{d_n}t\right) \tag{20}$$

where F_{tm} and F_{nm} are the maximum values of tangential and normal contact loads during impacts.

4) The kinetic friction coefficient μ_k is defined by:

$$\mu_k=\frac{F_{tm}}{F_{nm}} \tag{21}$$

Using Eq. (9) and assumptions 1. and 2., we obtain:

$$l_s=d_t\frac{(v_{it}+v_{rt})}{2} \tag{22}$$

where the tangential impact duration d_t is defined as the duration of application of tangential load during impact.

Combining Eqs. (1), (5), (6), (7), (8), we obtain:

$$l_s=d_t v_i\sin\alpha_i\left[\frac{1}{\tan\alpha_i}-\frac{\mu}{2}(1+e)\right] \tag{23}$$

In the case $\alpha_i\leq\alpha_c$, sliding occurs during all the contact, therefore $d_t=d_n$ and $\mu=\mu_k$. In the case $\alpha_i\geq\alpha_c$, a phase of sliding is followed by a phase during which $F_t=0$ and $F_n\neq0$, therefore $d_t\neq d_n$, $v_{rt}=0$ and $\mu=\mu_c$. It follows:

$$l_s=\begin{cases} d_n v_i\sin\alpha_i\left[\dfrac{1}{\tan\alpha_i}-\dfrac{\mu_k}{2}(1+e)\right], & \alpha<\alpha_c \\ d_t\dfrac{v_{it}}{2}=d_n v_i\cos\alpha_i\dfrac{1}{2\mu_k(1+e)\tan\alpha_i}, & \alpha>\alpha_c \end{cases} \tag{24}$$

The normal contact duration d_n is calculated following the case

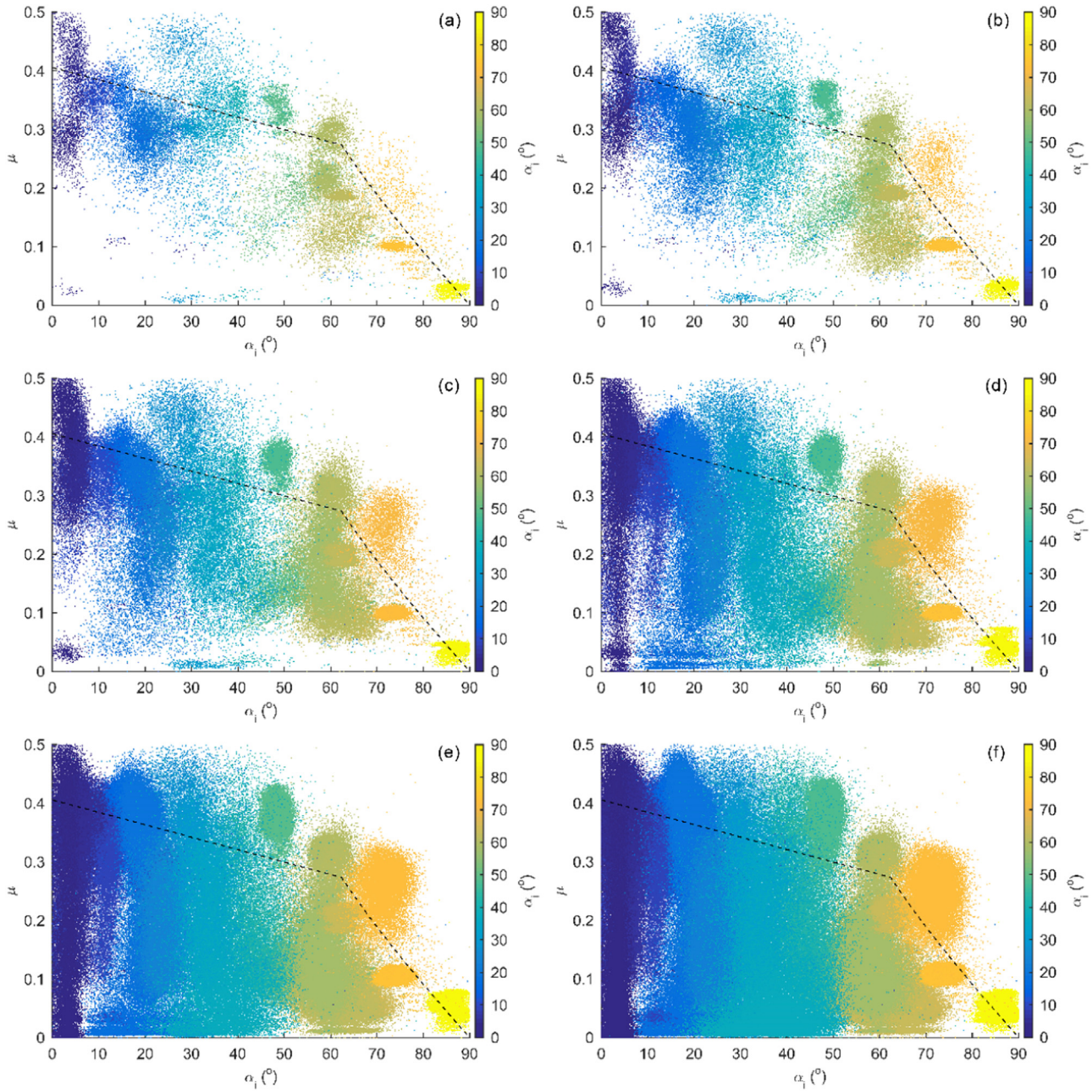

Fig. 8. Impulse ratio μ versus incidence angle α_i during long tests wear in water environment. Cloud: experimental data; dotted line computed from Eq. (16). (a) t=0–30 min. (b) t=0–1 h. (c) t=0–2 h. (d) t=0–4 h. (e) t=0–8 h. (f) t=0–16 h.

of an elastic shock between asperities considered as spheres [37]:

$$d_n = 2.87 \frac{m_a^{2/5}}{\left(\beta E^{*2} v_i \sin \alpha_i\right)^{1/5}} \quad (25)$$

where m_a is the apparent mass seen by one contact asperity, β the radius of curvature of the asperity and E^* the equivalent Young modulus of materials.

Finally, it leads to:

$$l_s = \begin{cases} 2.87 \frac{m_a^{2/5}}{\left(\beta E^{*2}\right)^{1/5}} \left(v_i \sin \alpha_i\right)^{4/5} \left[\frac{1}{\tan \alpha_i} - \frac{\mu_k}{2}(1+e)\right], & \alpha < \alpha_c \\ 2.87 \frac{m_a^{2/5}}{\left(\beta E^{*2}\right)^{1/5}} \left(v_i \sin \alpha_i\right)^{4/5} \frac{1}{2\mu_k (1+e) \tan^2 \alpha_i}, & \alpha > \alpha_c \end{cases} \quad (26)$$

The solid black curves in Fig. 6 and in Fig. 7 correspond to this model with equivalent Young modulus E^*=115GPa, incident velocity v_i=0. 07 m/s, asperity radius of curvature β = 100 μm and apparent mass respectively m_a=0.02 kg and m_a=0.05 kg. This difference of apparent mass seen by a contact asperity is related to a difference of contact asperities number during the two categories of tests carried and analyzed to draw Figs. 6 and 7. A good correlation is observed between the experimental values of sliding distance and the proposed model which tends to confirm the validity of this approach.

3.6. Scattering of measurements during long wear tests

Fig. 8 displays impulse ratio versus incidence angle for long wear tests during different time sequences selected in the complete duration of the tests. From the top left corner to bottom right corner, the sequences t=0–30 min (b), t=0–1 h (c), t=0–2 h (d), t=0–4 h (e), t=0–8 h (f), and t=0–16 h of each test are represented. Each color corresponds to a specific test with a constant incidence angle. The dotted black curve is computed from Eq. (16). Same evolutions of impact characteristics versus incidence angle and incident energy are observed during long wear tests with a progressive scattering of the measurements from the beginning of the test to the end. During the beginning of the long wear tests (t=0–1 h), the measurements are not substantially scattered and are well predicted by the model proposed in Eq. (16). The scattering progressively increases for the majority of the tests between t=1 h and t=20 h. In the specific case of Fig. 8, the impulse ratio decreases with time for the majority of the tests. This scattering of measurements with time seems to be linked to the contact geometry modification as wear is generated during long wear tests.

4. Wear analysis

4.1. Wear scars

At the end of each test, wear is observed on the SG tube and to a lesser extent on the AVB sample. Only SG tube wear is considered in the following as it constitutes the critical industrial issue. Fig. 9 displays a scanning electron microscope (SEM) image (a) and an interferometry image (b) of a typical wear scar obtained after 20 h of impacts in water environment. The global shape of the wear scar is triangular as the geometry of the contact is cylinder-plane with a small default of parallelism. The worn surface is globally smoother than the intact surface but presents also large cavities of length 500 μm and width 100 μm. Fig. 10 displays a magnification of the SEM image of Fig. 9. Numerous scratches of length 10–20 μm and width 1–2 μm are visible on the worn surface. This could correspond to the passage of an abrasive asperity or particle on the sample surface during an impact. It is interesting to note that the length of the observed scratches is in the same order of magnitude as the sliding distance during the impacts.

4.2. Wear roughness

The change of tube surface roughness properties between the undamaged and the worn surface visually observed in Figs. 9 and 10 is completed by an extensive analysis of the worn surface roughness parameters. For each test, the topography of the worn surface is measured using an interferometer and computed in order to obtain a mean value of the roughness parameter R_q. Fig. 11 displays the value of the impulse ratio μ_{end} at the end of each test versus the roughness parameter R_q. The impulse ratio increases from 0 to 0.45 when R_q increases from 0.22 to 1.58. In other words, a smooth worn surface leads to small values of impulse ratio. This result explains the measurements scattering observed in the previous section: during long wear tests, wear is generated, contact surfaces roughness decreases and therefore the impulse ratio decreases.

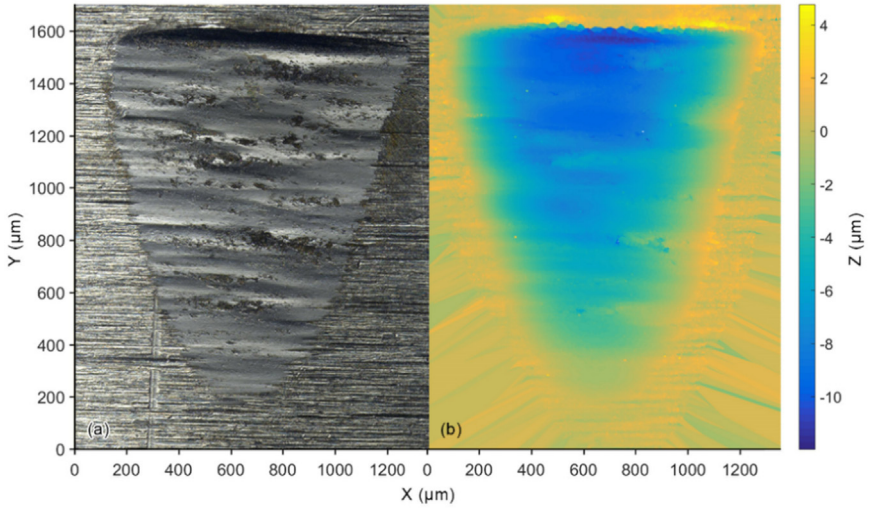

Fig. 9. Complete tube wear scar images. (a) SEM image. (b) Interferometry image.

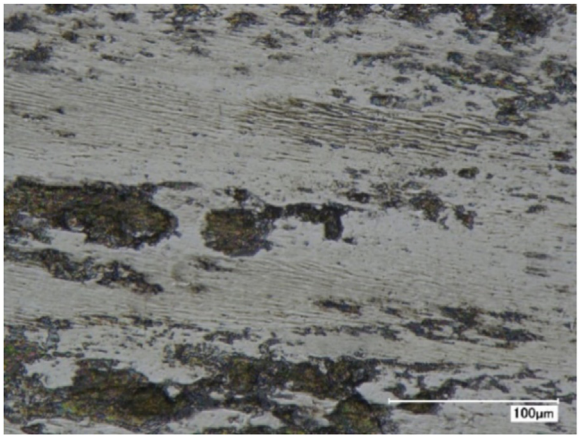

Fig. 10. Magnified tube wear scar SEM image.

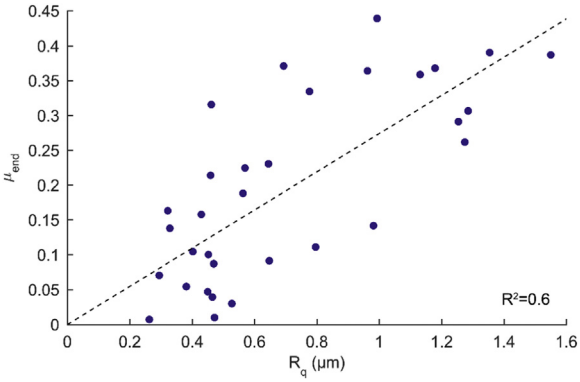

Fig. 11. Impulse ratio at the end of the wear test versus R_q roughness parameter of the wear scar; dotted black line: linear fit.

4.3. Wear volume

Fig. 12 displays experimental wear volume per impact versus average incidence angle for each long wear test carried out in water environment at constant incident energy. Wear increases from 3 to 5 µm^3 per impact between 5° and 20° and decreases from 5 to 0 µm^3 between 20° and 90°. Wear is maximum at 20° which is consistent with other studies on low-loaded percussive impacts [38–40]. The existence of a maximum of wear at a certain incidence angle is often observed in particle erosion studies [13,14,18]. This similarity shows that the same processes of material removal could happen for these two types of impacts. The validity of this argument is supported by the fact that the size and the energy of the projectile is at the same order of magnitude for

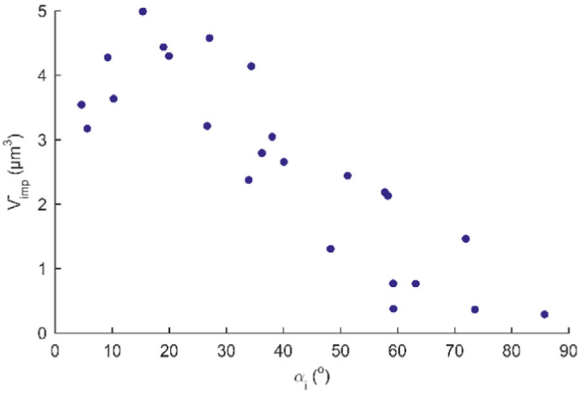

Fig. 12. Wear volume per impact versus incidence angle.

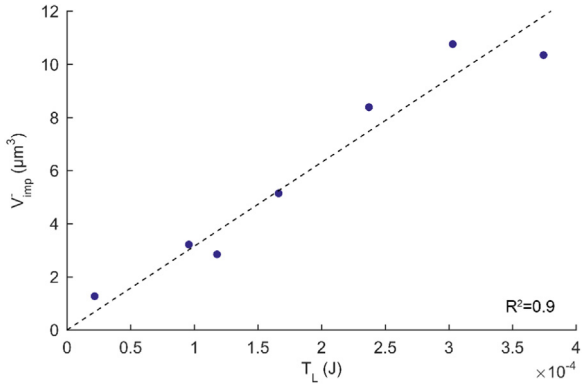

Fig. 13. Wear volume per impact versus energy loss at constant incidence angle equal to 30°; dotted black line: linear fit.

both cases: particle with high velocity but light mass for particle erosion and contact asperities with low velocity and high mass for low-loaded percussive impacts.

Fig. 13 displays experimental wear volume per impact versus average energy loss during impact for each long wear test carried out in water environment at constant incidence angle equal to 30°. Wear volume increases linearly with the energy loss from 0 to 12 µm^3 in the range 0–0.4 mJ. The dotted black curve is a linear fit of the experimental values. The observed proportionality between wear volume and energy loss during an impact is consistent with numerous studies [2,5,13,15,41–46]. It shows that a constant proportion of the energy loss is used to material removal in the range 0–0.4 mJ.

4.4. Discussion on energy

Fig. 14 displays wear volume per impact V_{imp}^{-} versus energy loss per impact T_L and mean incidence angle during the wear test α_i for each long wear test carried out in water environment. The color of the experimental points also corresponds to the incidence angle α_i. The four black curves correspond to four linear fits of the experimental values whose incidence angle ranges respectively from 5 to 15°, from 25 to 35°, from 50 to 60° and from 75 to 85°. For each of these ranges of incidence angle, a good proportionality is observed between wear volume V_{imp}^{-} and energy loss T_L. The proportionality coefficient K between wear volume and energy loss is different for each of these ranges and depends on the incidence angle:

$$V_{imp}^{-}=K(\alpha_i)T_L \tag{27}$$

A similar proportionality between wear volume and energy loss

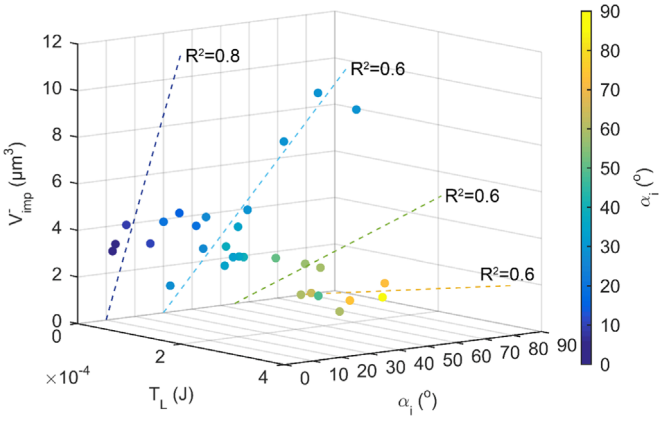

Fig. 14. Wear volume per impact versus impact energy loss and incidence angle; color: incidence angle; dotted lines: linear fits.

is observed for impacts in dry environment but with a proportionality coefficient independent of the incidence angle [32]. It shows that energy loss alone is not sufficient to predict impact wear volume in water environment: it depends both on energy loss and incidence angle. Therefore, the severest case for wear would be at low incidence angle and high energy loss. As energy loss is proportional to incident energy (Eq. (17)), the severest case for wear is at low incidence angle equal and high incident energy.

5. Conclusion

Wear induced by repetitive impacts between a steam generator tube sample and an anti-vibration bar sample in water environment is studied with a specific impact wear test machine. A statistical analysis of the impacts characteristics shows that the restitution coefficient slightly increases with the incidence angle. A two-parts evolution of the impulse ratio with incidence angle is observed and well predicted by the proposed model. The energy loss during impacts is measured and is found to be well predicted by Brach's formulation. The sliding distance during impacts is measured and well predicted by the proposed model.

Wear volumes and worn surface topography obtained after 20 h tests of 1.4 million impacts is deeply analyzed. A direct proportionality is observed between the final value of impulse ratio during a wear test and the worn surface roughness. Wear is observed to be proportional to energy loss with a proportionality coefficient strongly influenced by the incidence angle. The energy loss alone is observed to be insufficient to predict wear: wear depends on both incidence angle and energy loss.

References

[1] P.L. Ko, Metallic wear – a review with special references to vibration-induced wear in power plant components, Tribol. Int. 20 (1987) 66–78, http://dx.doi.org/10.1016/0301-679X(87)90092-2.

[2] P.A. Engel, Impact Wear of Materials, 2nd ed., Elsevier 1978 http://dx.doi.org/10.1115/1.3424343.

[3] P.A. Engel, Percussive impact wear. A study of repetitively impacting solid components in engineering, Tribol. Int. 11 (1978) 169–176, http://dx.doi.org/10.1016/0301-679X(78)90002-6.

[4] P.A. Engel, T.H. Lyons, J.L. Sirico, Impact wear model for steel specimens, Wear 23 (1973) 185–201, http://dx.doi.org/10.1016/0043-1648(73)90083-5.

[5] G. Levy, J. Morri, Impact fretting wear in CO2-based environments, Wear 106 (1985) 97–138, http://dx.doi.org/10.1016/0043-1648(85)90106-1.

[6] H.J. Connors, Flow-induced vibration and wear of steam generator tubes, Nucl. Technol. 55 (1981) 311–331, http://dx.doi.org/10.13182/NT55-311.

[7] T.M. Frick, An empirical wear projection technology with steam generator tube applications and relations to work-rate and wear simulations/tests, Flow.-Induc. Vib. Noise 2 (1997) 275–282.

[8] P.J. Hofmann, T. Schettler, D.A. Steininger, PWR steam generator tube fretting and fatigue wear phenomena and correlations, ASME Vib. Noise 1 (1992) 211–236.

[9] R. Lewis, A modelling technique for predicting compound impact wear, Wear 262 (2007) 1516–1521, http://dx.doi.org/10.1016/j.wear.2007.01.032.

[10] Y.B. Gessesse, On the Fretting Wear of Nuclear Power Plant Heat Exchanger Tubes Using a Fracture Mechanics Approach: Theory and Verification, Concordia University, Canada, 1997.

[11] H. Attia, A generalized fretting wear theory, Tribol. Int 42 (2009) 1380–1388, http://dx.doi.org/10.1016/j.triboint.2009.04.010.

[12] P. Shewmon, G. Sundararajan, The erosion of metals, Annu Rev. Mater. Sci. 13 (1983) 301–318, http://dx.doi.org/10.1146/annurev.ms.13.080183.001505.

[13] I. Finnie, Erosion of surfaces by solid particles, Wear 3 (1960) 87–103, http://dx.doi.org/10.1016/0043-1648(60)90055-7.

[14] I. Finnie, Some observations on the erosion of ductile metals, Wear 19 (1972) 81–90, http://dx.doi.org/10.1016/0043-1648(72)90444-9.

[15] J.G.A. Bitter, A study of erosion phenomena, Wear 6 (1963) 169–190, http://dx.doi.org/10.1016/0043-1648(63)90073-5.

[16] I.M. Hutchings, A model for the erosion of metals by spherical particles at normal incidence, Wear 70 (1981) 269–281, http://dx.doi.org/10.1016/0043-1648(81)90347-1.

[17] P.S. Follansbee, G.B. Sinclair, J.C. Williams, Modelling of low velocity particulate erosion in ductile materials by spherical particles, Wear 74 (1982) 107–122, http://dx.doi.org/10.1016/0043-1648(81)90197-6.

[18] S.B. Ratner, E.E. Styller, Characteristics of impact friction and wear of polymeric materials, Wear 73 (1981) 213–234, http://dx.doi.org/10.1016/0043-1648(81)90292-1.

[19] G. Sundararajan, P.G. Shewmon, A new model for the erosion of metals at normal incidence, Wear 84 (1983) 237–258, http://dx.doi.org/10.1016/0043-1648(83)90266-1.

[20] S. Jahanmir, N.P. Suh, Mechanics of subsurface void nucleation in delamination wear, Wear 44 (1977) 17–38, http://dx.doi.org/10.1016/0043-1648(77)90082-5.

[21] W.J. Stronge, Impact Mechanics., Cambridge University Press, 2000.

[22] R.M. Brach, Impact dynamics with applications to solid particle erosion, Int. J. Impact Eng. 7 (1988) 37–53, http://dx.doi.org/10.1016/0734-743X(88)90011-5.

[23] R.M. Brach, Classical planar impact theory and the tip impact of a slender rod, Int. J. Impact Eng. 13 (1993) 21–33, http://dx.doi.org/10.1016/0734-743X(93)90106-H.

[24] J. Guinot, Etude Bibliographique des Travaux Expérimentaux Menés sur l'usure par Impacts Glissements : Influence des Principaux Paramètres, 1989.

[25] S. Zaghdoudi, Analyse des Phénomènes d'usure par choc et Frottement, Université de Paris VI, 1992.

[26] P.L. Ko, Heat exchanger tube fretting wear: review and application to design, J. Tribol. 107 (1985) 149, http://dx.doi.org/10.1115/1.3261010.

[27] J.H. Cha, M.W. Wambsganss, J.A. Jendrzejczyk, Experimental study on impact/fretting wear in heat exchanger tubes, J. Press Vessel Technol. 109 (1987) 265–274, http://dx.doi.org/10.1115/1.3264862.

[28] R. Blevins, Vibration-induced wear of heat exchanger tubes, J. Eng. Mater. (1985) 107, http://dx.doi.org/10.1115/1.3225772.

[29] G.M. Sorokin, T.A. Polyanskaya, Machine for the investigations into the impact fatigue wear, Zavod Lab. 36 (1970) 611–612.

[30] S.L. Rice, Reciprocating impact wear testing apparatus, Wear 45 (1977) 85–95, http://dx.doi.org/10.1016/0043-1648(77)90104-1.

[31] R.J. Pick, K. Brown, A. Plumtree, Techniques in the study of impact and sliding wear of Zircaloy-4, Wear 52 (1979) 381–392, http://dx.doi.org/10.1016/0043-1648(79)90074-7.

[32] T. Souilliart, E. Rigaud, A. Le Bot, C. Phalippou, Energy-based wear law for oblique impacts in dry environment, Tribol. Int. 105 (2017) 241–249, http://dx.doi.org/10.1016/j.triboint.2016.10.014.

[33] Y. Kadmiri, E. Rigaud, J. Perret-Liaudet, L. Vary, Experimental and numerical analysis of automotive gearbox rattle noise, J. Sound Vib. 331 (2012) 3144–3157, http://dx.doi.org/10.1016/j.jsv.2012.02.009.

[34] T. Frick, T. Sobek, J. Reavis, Overview on the development and implementation of methodologies to compute vibration and wear of steam generator tubes, in: Proceedings ASME Symp, Flow-Induced Vib, vol. 3, Vib. Heat Exch., vol. 3,1984, pp. 149–161.

[35] F. Axisa, A. Desseaux, R. Gibert, Experimental study of tube/support impact forces in multi-span PWR steam generator tubes, Am. Soc. Mech. Eng. (1984).

[36] P. Hofmann, T. Schettler, N. Wieling, D.A. Steininger, Influence of contact conditions on vibration induced wear of metals, Nucl. Eng. Des. 119 (1990) 439–445, http://dx.doi.org/10.1016/0029-5493(90)90183-X.

[37] K.L. Johnson, Contact Mech. 19 (1984) 109–110, http://dx.doi.org/10.1016/0301-679X(86)90085-X.

[38] T. Souilliart, E. Rigaud, A. Le Bot, C. Phalippou Wear generated by sliding impacts, in: Proceedings Congrès Français Mécanique, Lyon, 2015, pp. 1–9.

[39] E. Rigaud, A. Le Bot, Influence of incidence angle on wear induced by sliding impacts, Wear 307 (2013) 68–74, http://dx.doi.org/10.1016/j.wear.2013.07.015.

[40] T. Souilliart, E. Rigaud, C. Phalippou, A. Le Bot, C. Phalippou, Wear Induced By Stochastic Sliding Impacts, in: Proceedings of the ASME 2015 Pressure Vessels and Piping Conference, Boston, ASME, 2015, pp. 1–6. ⟨http://dx.doi.org/10.1115/PVP2015-45811⟩.

[41] I.M. Hutchings, Deformation of metal surfaces by the oblique impact of square plates, Int. J. Mech. Sci. 19 (1977) 45–52, http://dx.doi.org/10.1016/0020-7403(77)90015-7.

[42] J.H. Neilson, A. Gilchrist, Erosion by a stream of solid particles, Wear 11 (1968) 111–122, http://dx.doi.org/10.1016/0043-1648(68)90591-7.

[43] G.P. Tilly, A two stage mechanism of ductile erosion, Wear 23 (1973) 87–96, http://dx.doi.org/10.1016/0043-1648(73)90044-6.

[44] G. Sundararajan, A comprehensive model for the solid particle erosion of ductile materials, Wear 149 (1991) 111–127, http://dx.doi.org/10.1016/0043-1648(91)90368-5.

[45] K. Wellinger, H. Breckel, Kenngrössen und verschleiss beim stoss metallischer werkstoffe, Wear 13 (1969) 257–281, http://dx.doi.org/10.1016/0043-1648(69)90249-X.

[46] R. Fricke, C. Allen, Repetitive impact wear of steels, Wear 164 (1993) 837–847, http://dx.doi.org/10.1016/0043-1648(93)90085-Z.